



# Testing He II Emission from Wolf–Rayet Stars as a Dust Attenuation Measure in Eight Nearby Star-forming Galaxies

Daniel Maschmann<sup>1</sup> , Claus Leitherer<sup>2</sup> , Andreas L. Faisst<sup>3</sup> , Janice C. Lee<sup>1,2,4</sup> , and Rebecca Minsley<sup>1</sup>

<sup>1</sup> Steward Observatory, Department of Astronomy, University of Arizona, 933 N. Cherry Avenue, Tucson, AZ 85721, USA; [danielmaschmann@arizona.edu](mailto:danielmaschmann@arizona.edu)

<sup>2</sup> Space Telescope Science Institute, 3700 San Martin Drive, Baltimore, MD 21218, USA

<sup>3</sup> Caltech-IPAC, 1200 E. California Boulevard, Pasadena, CA 91125, USA

<sup>4</sup> Gemini Observatory/NSF's NOIRLab, 950 N. Cherry Avenue, Tucson, AZ, 85719, USA

Received 2023 September 25; revised 2023 November 22; accepted 2023 November 28; published 2024 January 23

## Abstract

The ability to determine galaxy properties such as masses, ages, and star formation rates robustly is critically limited by the ability to measure dust attenuation accurately. Dust reddening is often characterized by comparing observations to models of either nebular recombination lines or the UV continuum. Here, we use a new technique to measure dust reddening by exploiting the He II  $\lambda 1640$  and  $\lambda 4686$  emission lines originating from the stellar winds of Wolf–Rayet stars. The intrinsic line ratio is determined by atomic physics, enabling an estimate of the stellar reddening similar to how the Balmer lines probe gas-emission reddening. The He II line ratio is measured from UV and optical spectroscopy using the Space Telescope Imaging Spectrograph on board the Hubble Space Telescope for eight nearby galaxies hosting young massive star clusters. We compare our results to dust reddening values estimated from UV spectral slopes and from Balmer line ratios and find tentative evidence for systematic differences. The reddening derived from the He II lines tends to be higher, whereas that from the UV continuum tends to be lower. A larger sample size is needed to confirm this trend. If confirmed, this may indicate an age sequence probing different stages of dust clearing. Broad He II lines have also been detected in galaxies more distant than in our sample, providing the opportunity to estimate the dust reddening of the youngest stellar populations out to distances of  $\sim 100$  Mpc.

*Unified Astronomy Thesaurus concepts:* Star formation (1569); Star clusters (1567); Interstellar dust extinction (837); Wolf-Rayet stars (1806)

## 1. Introduction

Dust is a constant companion of star formation, since it is not only a component of the clouds that collapse to stars, but is also reinjected into the interstellar medium (ISM) by feedback mechanisms providing material for the next stars to form. It is therefore of great importance to quantify dust in star-forming regions and young star clusters in order to be able to determine properties such as star formation rates, masses, ages, or metallicities (Calzetti 2009). Light passing through dust clouds is attenuated, where the intensity of the attenuation depends on the wavelength. Specifically, the bluer part of a spectrum is more strongly attenuated compared to the red, hence the spectral energy distributions are reddened. Reddening is quantitatively described by dust attenuation curves (Fitzpatrick 1986; Calzetti et al. 1994; Salim et al. 2018). In practice, dust attenuation is measured by comparing observations with model predictions either through the stellar UV continuum (e.g., Calzetti et al. 1994) or recombination line ratios of hydrogen (e.g., Domínguez et al. 2013). In this work we aim to test an alternative method to estimate dust reddening in nearby galaxies relying on stellar He II emission lines. Two lines are of special interest: He II  $\lambda 1640$  and  $\lambda 4686$  as they can be observed in the local Universe with UV and optical spectroscopy, respectively. These lines are prevalent as nebular recombination lines in the presence of a hard ionizing source (ionization energy of  $\text{He}^+$  is 54.4 eV) such as an active galactic nucleus or stellar sources such as X-ray binaries in H II regions

(Shirazi & Brinchmann 2012). They also occur in stellar winds surrounding Wolf–Rayet (W-R) stars. Their large line widths due to high wind velocities uniquely distinguish them from nebular emissions (Schaerer 1996). The stellar He II  $\lambda 1640$  and  $\lambda 4686$  lines can be considered as almost pure recombination lines, and thus their intrinsic flux ratio is determined by atomic processes. This ratio decreases due to dust attenuation enabling a stellar dust reddening estimate, first proposed by Conti & Morris (1990). The theoretical value is predicted to be 8.36 for an electron density of  $n_e = 10^9 \text{ cm}^{-3}$ , an electron temperature of  $T_e = 20,000 \text{ K}$ , and Case B recombination (Hummer & Storey 1987), which are representative for stellar winds in W-R stars. Crowther & Hadfield (2006) estimated the line ratio to be of the order of 10 from stellar atmosphere models for all types of W-R stars of the nitrogen sequence (WN). Based on stellar models, Schaerer & Vacca (1998) found average line ratios of 7.55 and 7.95 for late WN stars in the Galaxy and the Large Magellanic Cloud (LMC), respectively. By using reddening corrected line fluxes, Leitherer et al. (2019) empirically estimated an intrinsic He II  $\lambda 1640$  to  $\lambda 4686$  line ratio of 7.76 from W-R stars in the Galaxy and the LMC. As the latter estimate does not suffer from systematics due to model choices, we adopt this value throughout this work.

One of the main motivations to use recombination lines emitted by W-R stars as a dust tracer is that this method only probes the youngest stellar populations in a very specific evolutionary phase. W-R stars mainly appear in the first 5 Myr, whereas the W-R phase of a star lasts for  $< 1$  Myr (Meynet & Maeder 2005). They can be the result of a single O-type star evolving into a W-R star (Meynet et al. 2017) or through mass transfer in a binary star system (Eldridge et al. 2017). In metal-rich environments (approximately solar metallicity), W-R stars



Original content from this work may be used under the terms of the [Creative Commons Attribution 4.0 licence](https://creativecommons.org/licenses/by/4.0/). Any further distribution of this work must maintain attribution to the author(s) and the title of the work, journal citation and DOI.

can be produced at later times  $\sim 10$  Myr, whereas in metal-poor environments (subsolar metallicity) no W-R stars are expected after 5 Myr (see Figure 14 in Leitherer et al. 2014). In this work we can assume the latter case as the galaxy sample has subsolar metallicity (see Table 1 in Chandar et al. 2004). The only exception is the galaxy He 2–10. However, the estimated age of the region studied here is 5 Myr (see Table 2 in Chandar et al. 2004). In our Galaxy and the Magellanic Clouds W-R stars are studied extensively by means of their large variety of spectroscopic features (Crowther 2007). The occurrence rate of W-R stars depends on the ISM metallicity (Conti et al. 1983; van der Hucht 2001), which also has a great impact on their spectroscopic features (Mokiem et al. 2007). It is important to emphasize that the origin of W-R stars is not important for the present study. The He II ratios are not affected by the type or evolution of the W-R stars, the initial mass function, or the metallicity (Leitherer et al. 2019). However, an important requirement of this method is the need of sufficiently high spectral resolution in order to distinguish broad from narrow He II lines.

The ages quoted above are based on single-star models. For binary star systems on the other hand, these timescales are longer: mass transfer in binaries can lead to hydrogen-free (or hydrogen-deficient) stars after 5 Myr. These stars would be classified as W-R (Xiao et al. 2018). Furthermore, recent discoveries of intermediate-mass helium dwarfs (Drout et al. 2023; Göteborg et al. 2023) suggest that there is in fact a continuum of stripped stars from W-R stars to intermediate-mass helium dwarfs. However, these stars do not indicate strong emission lines, which makes it unlikely that broad He II lines trace populations older than  $\sim 5$  Myr. Furthermore, the ages of the targets we are using in this study are estimated to be  $\leq 7$  Myr (Chandar et al. 2004, their Table 2).

We have chosen a sample of eight galaxies hosting bright and massive young star clusters. We observed these sources with the Space Telescope Imaging Spectrograph (STIS), on board the Hubble Space Telescope (HST) at UV and optical wavelengths using narrow apertures ( $0''.2$  and  $0''.5$ ). These observations also enable us to use the UV slope as a stellar dust estimator and compare our results. In addition, we use Balmer line measurements from the literature to compare dust reddening values of stellar and nebula origin.

The remainder of this paper is organized as follows. In Section 2 we describe the nearby galaxy sample targeted for UV–optical spectroscopy with HST/STIS. We also summarize the observations, and describe the steps taken to reduce the data. In Section 3, we describe existing data used in our analysis: spectroscopy with the Multi Unit Spectroscopic Explorer (MUSE) on the Very Large Telescope (VLT) and the Sloan Digital Sky Survey (SDSS), as well as measurements reported in the literature. In Section 4, the procedures used to calculate  $E(B - V)$  from the He II line ratio, Balmer line ratio, and UV continuum are discussed. In Section 5, we compare the reddening as computed from all three methods, and find general agreement. We discuss the potential for measuring dust attenuation using the He II line ratio in higher-redshift galaxies. Finally, we provide a summary of our analysis and results in Section 6.

## 2. Observations

To measure dust attenuation through broad He II lines outside the Local Group of galaxies, high-quality spectroscopic

observations in the UV and optical wavelength range are needed. In addition, both observations must have cospatial apertures as to probe the emission at the same spatial location. Therefore, the target sample has to be selected from known extragalactic nearby H II regions containing W-R stars, and the spectra used for the subsequent analysis need to be cospatial.

### 2.1. Target Sample

For this study, we selected star-forming regions in eight nearby galaxies ( $0.0010 \lesssim z \lesssim 0.0095$ , at distances of 3–37 Mpc) with existing He II  $\lambda 1640$  HST/STIS UV observations from the Mikulski Archive for Space Telescopes (MAST). These UV spectra were previously obtained for He 2–10, NGC 3125, Mrk 33, NGC 4214, NGC 4670, and Tol 1924–416 as part of program 9036 (PI: C. Leitherer) taken in 2001–2003, and for NGC 3049 and Tol 89 as part of program 7513 (PI: C. Leitherer) observed in 1999–2000. Additional optical HST/STIS observations, providing He II  $\lambda 4686$  line measurements were obtained from the HST program GO-15846 (PI: C. Leitherer), executed in 2020–21. These optical observations were carried out at the exact same location, same orientation, and with the same aperture sizes as the UV observations. This is crucial for comparing the UV and optical measurements of the same stellar regions in the galaxies. Furthermore, space-based observations are invaluable for reaching the necessary spatial resolution. A detailed description of the reduction of these new data is provided in Section 2.3.

The analysis of galaxies in program 9036 was published in Chandar et al. (2004) and Chandar et al. (2005), quantifying the W-R and O-star content for selected massive young star clusters and to understand better the strong He II  $\lambda 1640$  features observed in Lyman-break galaxies (LBGs) at redshifts  $z \sim 3$ . An analysis of the UV spectra of NGC 3049 was published in González Delgado et al. (2002) with the goal of studying massive stars in metal-rich starbursts and performing consistency tests of existing starburst models for such high-metallicity environments. The giant H II region Tol 89 in NGC 5398 was analyzed in Sidoli et al. (2006) with supplementary HST imaging and VLT/Ultraviolet and Visual Echelle Spectrograph (UVES) spectroscopy. They resolve the substructure of this region and identified super star clusters based on spectral modeling. These eight selected galaxies are widely studied and well known for their young massive star-forming regions and therefore form an excellent sample to study their He II emission line properties. In Table 1, we present the most important characteristics such as coordinates, redshift, and Galactic extinction values, and the STIS aperture widths for the galaxies.

The present work is a pilot program to test the application of He II lines as dust tracers in nearby galaxies, thus, the sources were selected as the strongest He II emitters. In particular, NGC 3125 is known to be the strongest He II  $\lambda 1640$  source in the local Universe (Chandar et al. 2004) and therefore provides excellent conditions to test these mechanisms. Furthermore, some of the selected targets have multiple sources covered with STIS slit pointing. He 2–10 contains four strong sources, with sufficient spatial separation for an individual spectral analysis of each of them. Mrk 33, NGC 3049, and NGC 4670 also have multiple sources, but as described in Section 2.3, the measured He II lines suffer from low signal-to-noise ratio (S/N) values

**Table 1**  
Galaxy Sample

Galaxy	R.A.	Decl.	$z$	$A_V$ (Gal.)	Slit Width	Total Exp	
						G140L (s)	G430M (s)
He 2–10	08 <sup>h</sup> 36 <sup>m</sup> 15 <sup>s</sup> .13	−26°24′33″.7	0.0029	0.31	0.2	10891	4195
NGC 3049	09 <sup>h</sup> 54 <sup>m</sup> 49 <sup>s</sup> .40	+09°16′15″.9	0.0049	0.11	0.5	11064	1650
NGC 3125	10 <sup>h</sup> 06 <sup>m</sup> 33 <sup>s</sup> .29	−29°56′06″.8	0.0037	0.21	0.2	3975	4084
Mrk 33	10 <sup>h</sup> 32 <sup>m</sup> 31 <sup>s</sup> .88	+54°24′02″.2	0.0048	0.03	0.2	1446	4084
NGC 4214	12 <sup>h</sup> 15 <sup>m</sup> 39 <sup>s</sup> .45	+36°19′34″.8	0.0010	0.06	0.2	1544	4235
NGC 4670	12 <sup>h</sup> 45 <sup>m</sup> 17 <sup>s</sup> .44	+27°07′31″.8	0.0036	0.04	0.2	1470	4090
Tol 89	14 <sup>h</sup> 01 <sup>m</sup> 19 <sup>s</sup> .92	−33°04′10″.7	0.0041	0.18	0.5	11620	1650
Tol 1924-416	19 <sup>h</sup> 27 <sup>m</sup> 58 <sup>s</sup> .31	−41°34′29″.8	0.0095	0.24	0.2	4044	4108

**Note.** Redshifts and Galactic  $A_V$  are taken from the NASA/IPAC Extragalactic Database. We further list the STIS slit widths and the exposure times.

and only one source will ultimately provide a He II  $\lambda 1640$  to  $\lambda 4686$  line ratio.

## 2.2. HST/STIS Observations

The UV HST/STIS spectra were taken in the far-ultraviolet (FUV) using the Multianode Microchannel Array (FUV-MAMA) detector with the STIS G140L grating; the optical spectra were taken with the G430M grating with the STIS/CCD. The G140L grating covers the wavelength range 1150–1730 Å, with a dispersion of 0.6 Å pixel<sup>−1</sup> and a pixel scale of  $\sim 0''.025$  pixel<sup>−1</sup>. Spectra obtained with the G430M grating cover a wavelength range and dispersion of 4563–4849 Å and 0.28 Å pixel<sup>−1</sup>, respectively. The pixel scale for all optical spectra is  $\sim 0''.051$  pixel<sup>−1</sup>.

A prerequisite for our analysis is that our observations are cospatial at UV and optical wavelengths. At the outset of our analysis we therefore confirmed that the orientation of the slit was identical across the three gratings for all targets. The STIS instrument target acquisition process is done in three main parts. The first two involve centering the target in a  $100 \times 100$  pixel target acquisition subarray. After the initial guide star acquisition, the instrument makes an initial pointing whereby the target is captured within the acquisition subarray. The instrument then does a coarse centering in which the target is placed with respect to a reference point in the target acquisition subarray. The third step performs the fine centering, which places the object precisely within the slit. In Figure 1, we show the slit positions of both observations superposed on existing HST image observations.

## 2.3. STIS Data Reduction

We identify the spectral traces of massive star-forming regions on the observed 2D STIS images and convert them to 1D spectra. The goal is to measure the He II  $\lambda 1640$  and  $\lambda 4686$  line fluxes in the G140L and G430M spectra, respectively, on which a subsequent dust attenuation estimate is based. Furthermore, we estimate the slope of the UV continuum emission in the G140L spectra, providing an independent measurement of the stellar dust attenuation.

All STIS data are retrieved from the MAST and further processed using the CALSTIS pipeline (see Sohn 2019). The basic 2D image processing steps done by the pipeline differ slightly depending on the detector used to observe the data (MAMA or CCD). The basic 2D image module (*basic2d*)

consists of the following tasks: bad pixel flagging, conversion of native high-resolution pixels to low-resolution pixels (MAMA), global linearity correction (MAMA), overscan and bias subtraction (CCD), dark subtraction, flat-field corrections, and wavelength calibration. The pipeline also includes cosmic-ray rejection used for CCD-recorded data. For targets with multiple exposures, we check for any spatial offsets between exposures (none were found to have  $>0.25$  pixel offsets) and coadd the raw data files before processing them with the CALSTIS pipeline. The total exposure times across all observations are given in Table 1.

The 2D spectral images are used to identify the spectral traces of the bright star-forming regions. The width of the extraction box is identified by eye to include the total flux and at the same time minimize contamination from neighboring sources. The extraction box pixel sizes are slightly larger for the UV spectra (9–19 pixels), in comparison to the optical spectra (5–9 pixels) due to the smaller pixel size of the STIS FUV-MAMA detector compared to that of the CCD detector. We use the `x1d` `ststools` function to extract the 1D data. This function automatically calculates and subtracts the background, corrects the wavelengths to a heliocentric reference frame, and does the absolute flux calibration. We then convert the observed wavelength to rest-frame wavelength using the redshift measurement from the spectrum. The G140L spectra and the He II  $\lambda 1640$  and  $\lambda 4686$  lines are shown for each identified source in Figure 2. As a final step, all spectra are visually inspected to identify and manually remove detector flaws. This is for example the case for the G430M spectrum of the target Mrk 33-B at around 4675 Å rest-frame wavelength. A cosmic ray in the flat field was not detected by the pipeline and therefore was not properly flagged. In this case, the corresponding wavelength was flagged and removed in the subsequent analysis.

We first measure the UV continuum slope  $\beta$  by fitting a linear function to the data points between 1240 and 1700 Å. In order to avoid absorption and emission features, the fit only considers specific wavelength intervals as specified in Calzetti et al. (1994). We deredden the flux to account for Milky Way extinction using the Cardelli et al. (1989) reddening law before measuring the UV slope. The best fit to the continuum data points is shown for each spectrum in Figure 2, and the measured  $\beta$ -values are listed in Table 2.

Subsequently, we use the estimated UV continuum to determine the He II  $\lambda 1640$  line flux from the continuum-



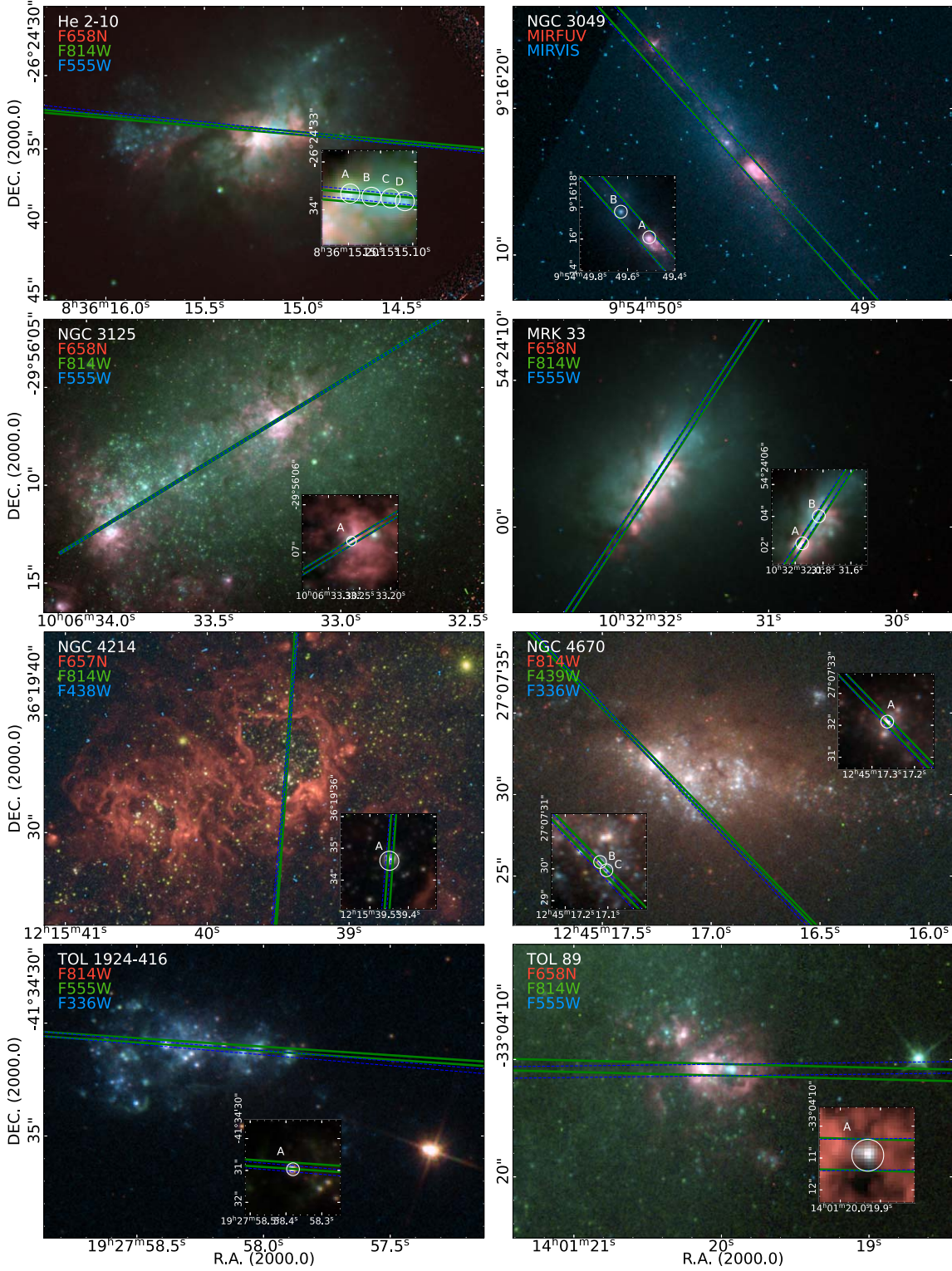


**Figure 1.** Observed galaxies with STIS slit positions overlaid. For each galaxy we show HST composite images taken from the archive using the software MULTICOLORFITS (<https://github.com/pjcigan/multicolorfits>) and include the aligned STIS slits with a solid green (dashed blue) line for the G140L (G430M) grating. The zoom-in panels show the identified He II emitters.

subtracted spectra. To measure the He II  $\lambda 4686$  line flux, we subtract the continuum, estimated with a linear fit between 4600 and 4800 Å, excluding regions with known emission lines. The line fluxes are measured by summing up the flux between 1631 and 1652 Å for the He II  $\lambda 1640$  line and between

4670 and 4705 Å for the He II  $\lambda 4686$  line. Note that the latter are blended with [Fe III]  $\lambda 4658$  and other stellar lines, whose ratios depend on the types of W-R stars present. The wavelength range is chosen based on the width of He II  $\lambda 1640$ , which is expected to be comparable to the width of

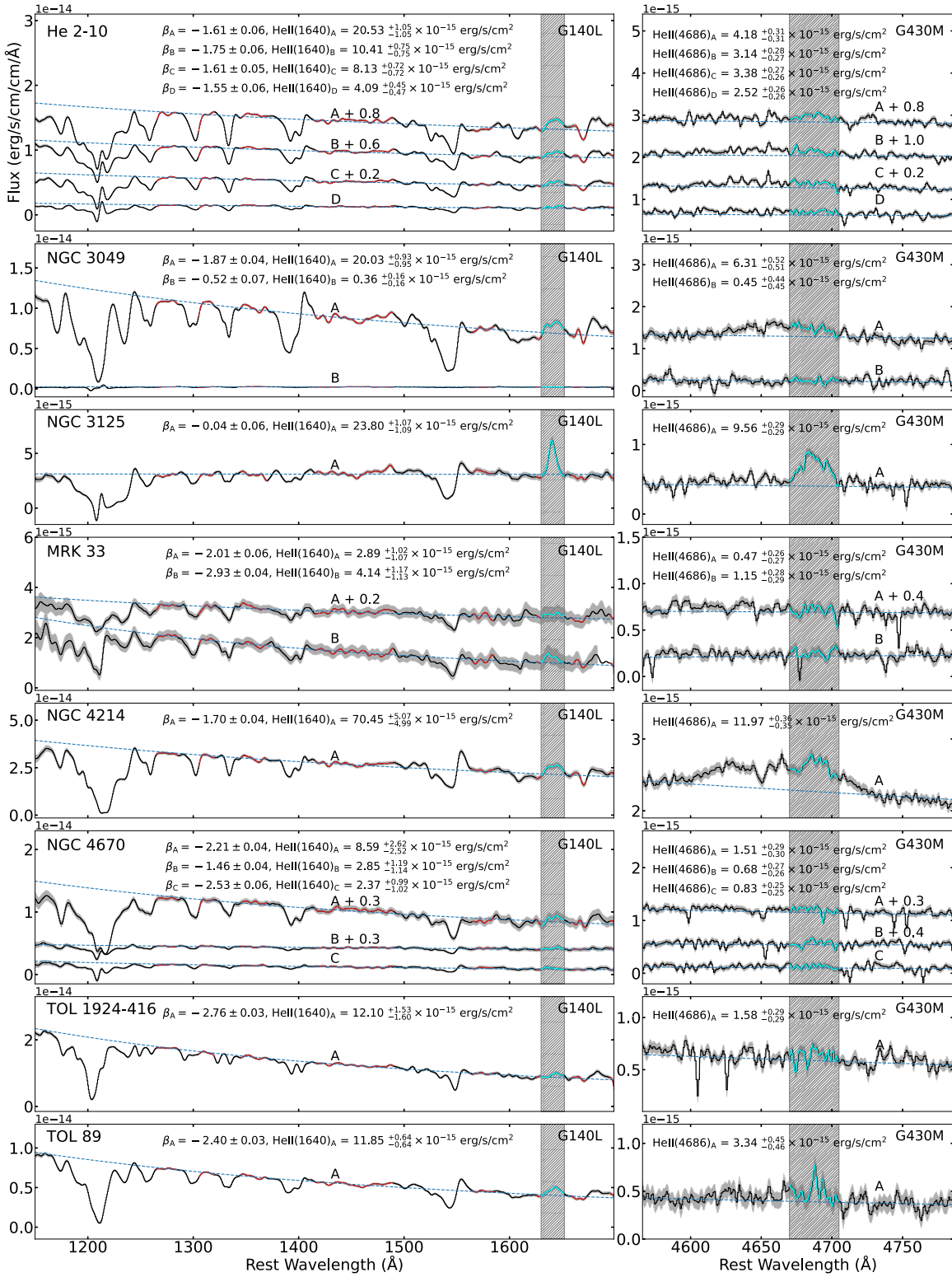


**Figure 2.** Extracted STIS spectra for the G140L grating and the He II  $\lambda 4686$  line in the G430M grating. For each galaxy, we display the spectra of all identified He II emitters. For multiple spectra we add an offset to distinguish them. We show the continuum fit with blue dashed lines. The data points used for the continuum fit for the G140L grating are marked in red. The wavelength windows for the He II  $\lambda 1640$  and  $\lambda 4686$  lines are marked with a gray background and the lines are highlighted in turquoise. The measured quantities for each spectrum are displayed on the top and also summarized in Table 2.

He II  $\lambda 4686$  (Hillier 1987; Leitherer et al. 2019). We estimate the line uncertainties with a Monte Carlo approach by randomly adding Gaussian noise with the scale of the measured noise level in the selected region. We repeat this 1000 times and compute the uncertainties as the 68th percentile.

### 3. Balmer Line Measurements

In addition to reddening estimates based on He II lines and the UV slope, alternative tracers can be used for comparison. Balmer recombination lines emitted from H II regions are one

**Table 2**  
*E(B − V)* Measurements

Target		$F(1640)$ ( $10^{-15}$ erg s $^{-1}$ cm $^{-2}$ )	$F(4686)$	$F1640/F4686$	$\beta$	$E(B - V)_{\text{He II}}$ (mag)	$E(B - V)_{\text{UV Slope}}$ (mag)	$E(B - V)_{\text{Balmer}}$ (mag)
HE 2–10	A	$20.5 \pm 1.0$	$4.2 \pm 0.3$	$4.9 \pm 0.4$	$-1.6 \pm 0.1$	$0.10 \pm 0.02$	$0.18 \pm 0.01$	$0.13 \pm 0.01$
	B	$10.4 \pm 0.7$	$3.1 \pm 0.3$	$3.3 \pm 0.3$	$-1.8 \pm 0.1$	$0.18 \pm 0.02$	$0.15 \pm 0.01$	$0.17 \pm 0.01$
	C	$8.1 \pm 0.7$	$3.4 \pm 0.3$	$2.4 \pm 0.2$	$-1.6 \pm 0.1$	$0.25 \pm 0.02$	$0.18 \pm 0.01$	$0.12 \pm 0.01$
	D	$4.1 \pm 0.5$	$2.5 \pm 0.3$	$1.6 \pm 0.2$	$-1.6 \pm 0.1$	$0.34 \pm 0.03$	$0.20 \pm 0.01$	$0.22 \pm 0.01$
NGC 3049	A	$20.0 \pm 0.9$	$6.3 \pm 0.5$	$3.2 \pm 0.3$	$-1.9 \pm 0.0$	$0.19 \pm 0.02$	$0.13 \pm 0.01$	$0.29 \pm 0.03$
	B	$0.4 \pm 0.2$	$0.5 \pm 0.4$	...	$-0.5 \pm 0.1$	...	$0.42 \pm 0.02$	$0.29 \pm 0.03$
NGC 3125	A	$23.8 \pm 1.1$	$9.6 \pm 0.3$	$2.5 \pm 0.1$	$-0.0 \pm 0.1$	$0.25 \pm 0.01$	$0.53 \pm 0.01$	$0.03 \pm 0.01$
MRK 33	A	$2.9 \pm 1.0$	$0.5 \pm 0.3$	...	$-2.0 \pm 0.1$	...	$0.09 \pm 0.01$	$0.01 \pm 0.01$
	B	$4.1 \pm 1.1$	$1.2 \pm 0.3$	$3.6 \pm 0.9$	$-2.9 \pm 0.0$	$0.17 \pm 0.06$	$-0.11 \pm 0.01$	$0.01 \pm 0.01$
NGC 4214	A	$70.4 \pm 5.0$	$12.0 \pm 0.4$	$5.9 \pm 0.2$	$-1.7 \pm 0.0$	$0.06 \pm 0.01$	$0.16 \pm 0.01$	$0.06 \pm 0.02$
NGC 4670	A	$8.6 \pm 2.6$	$1.5 \pm 0.3$	$5.7 \pm 1.2$	$-2.2 \pm 0.0$	$0.07 \pm 0.04$	$0.05 \pm 0.01$	$0.15 \pm 0.03$
	B	$2.9 \pm 1.2$	$0.7 \pm 0.3$	...	$-1.5 \pm 0.0$	...	$0.21 \pm 0.01$	$0.15 \pm 0.03$
	C	$2.4 \pm 1.0$	$0.8 \pm 0.3$	...	$-2.5 \pm 0.1$	...	$-0.02 \pm 0.01$	$0.15 \pm 0.03$
TOL 89	A	$11.9 \pm 0.6$	$3.3 \pm 0.5$	$3.6 \pm 0.5$	$-2.4 \pm 0.0$	$0.17 \pm 0.03$	$0.01 \pm 0.01$	$0.07 \pm 0.01$
TOL 1924-416	A	$12.1 \pm 1.6$	$1.6 \pm 0.3$	$7.6 \pm 1.4$	$-2.8 \pm 0.0$	$0.00 \pm 0.04$	$-0.07 \pm 0.01$	$-0.069 \pm 0.002$
	B	$-1.0 \pm 0.5$	$0.7 \pm 0.3$	...	$-1.1 \pm 0.1$	...	$0.28 \pm 0.02$	$-0.069 \pm 0.002$

**Note.** We show the He II  $\lambda 1640$  and  $\lambda 4686$  line flux, their ratio, and the measured UV slope  $\beta$  for all STIS spectra. For targets with line fluxes with  $S/N < 3$  we do not calculate the line ratio. We furthermore list the calculated  $E(B - V)_{\text{He II}}$  and  $E(B - V)_{\text{UV}}$ , as well as the dust reddening estimations from Balmer lines  $E(B - V)_{\text{Balmer}}$ . As described in Section 3, in some cases no individual  $E(B - V)_{\text{Balmer}}$  values are estimated for multiple targets in one galaxy due to larger spectral apertures. In such a case we use the same Balmer line estimate for all targets within one galaxy.

of the most commonly used tools for reddening estimates (e.g., Domínguez et al. 2013; Momcheva et al. 2013). For the present sample, we collected Balmer line observations from the VLT/MUSE, SDSS, and individual spectroscopic estimates from the literature.

### 3.1. Archival MUSE Observations

Due to its high spatial resolution, MUSE observations are well suited to estimate Balmer line fluxes for the regions observed with STIS. We selected archival MUSE observations performed in the wide-field mode from the ESO Archive for He 2-10 (ID: 095.B-0321), NGC 3125 (ID: 094.B-0745), and Tol 1924-416 (ID: 60.A-9314). The spatial resolution for each target is below  $1''$  (taking the individual seeing into account) and covers the optical wavelengths from 4650 to 9300 Å, which includes the H $\beta$  and H $\alpha$  lines. To identify the correct region of He II emitters, we aligned the MUSE observations with the HST imaging observations, which we had previously aligned with the STIS observations (See Section 2 and Figure 1). In order to align the MUSE data cube properly, we cross-identified three to six point-like bright clusters or H II regions in both MUSE and HST imaging, and calculated a new solution for the world coordinate system of the MUSE observation. This alignment is crucial to select the same stellar regions as with the HST/STIS observations.

Considering the STIS slit width of  $0''.2$ , the spatial resolution of MUSE is insufficient to resolve properly multiple sources which are aligned along the STIS slit as we find for He 2–10. In this case all four identified He II emitters are located within  $1''$ . Even though the spectra are cross-contaminated due to the point-spread function and the seeing, we select each source individually, which is made possible by the MUSE pixel size of  $0''.2 \times 0''.2$ .

The He II emitter in the galaxy Tol 1924-416 is fairly isolated and has a diameter of  $0''.5$ , excluding most possible sources of contamination. For the H II region in NGC 3125, on the other hand, the spectral selection is not so straight forward.

In fact this region is so bright that in the central part of the region the H $\alpha$  emission is saturated in the MUSE observations. In order to estimate the Balmer lines from this region, we only select the surrounding unsaturated pixels within a radius of  $0''.5$ .

### 3.2. Archival SDSS Spectra

Spectroscopic observations from SDSS are integrated over a circular aperture of  $3''$  and cover the wavelength range from 3800 to 9200 Å, enabling measurements of the H $\gamma$ , H $\beta$ , and H $\alpha$  lines. We found SDSS spectral observations for Mrk 33, NGC 3049, and NGC 4670 centered on massive star formation regions, which are among our targets. Despite the difference in aperture between the STIS and the SDSS observations, these provide a good estimate assuming most of the nebular emission comes from the selected young star cluster regions. For the galaxy Mrk 33, the H $\alpha$  emission line is saturated in the SDSS spectra, and we therefore use the H $\beta$  and H $\gamma$  ratio to estimate the Balmer decrement.

### 3.3. Balmer Line Observations in the Literature

The massive star-forming region Tol 89 in NGC 5398 was observed with VLT/UVES by Sidoli et al. (2006). These observations are cospatial with the STIS observations and therefore provide a precise measurement of the Balmer decrement estimated from their estimated H $\alpha$  and H $\beta$  line fluxes.

For NGC 4214, we use archival spectra provided by Moustakas & Kennicutt (2006), who observed this target with a long slit by drifting over the entire galaxy. These observations only provide a global estimate of the Balmer decrement, which can be seen as an average of the galaxy and not as representative of the relatively small region probed by the STIS observations.



#### 4. Reddening Estimates

Dust in the ISM causes wavelength-dependent attenuation. Specifically, the slope of the stellar UV continuum and the ratio of emission lines situated at different wavelengths change. Recombination lines, such as the Balmer line series, have a known intrinsic ratio determined by atomic physics and the  $n_e$  and  $T_e$  of the H II region. The novelty of this work is to test the estimate of dust attenuation based on stellar (as opposed to nebular) He II lines, calibrated in Leitherer et al. (2019). In order to evaluate this method we compare the resulting  $E(B - V)$  values to estimates based on the stellar UV continuum and nebular Balmer lines.

##### 4.1. Reddening Estimates Based on He II $\lambda 1640$ and $\lambda 4686$

The ratio between the stellar He II  $\lambda 1640$  and  $\lambda 4686$  lines is a fixed value. Following Leitherer et al. (2019) the intrinsic ratio is

$$R_0 = \frac{F_0(1640)}{F_0(4686)}, \quad (1)$$

where  $F_0(1640)$  and  $F_0(4686)$  are the reddening-free line fluxes. This ratio ( $R_{\text{obs}}$ ) decreases because of the effects of dust attenuation. The observed, reddened and the intrinsic, unreddened ratio are related as

$$\frac{R_{\text{obs}}}{R_0} = 10^{0.4 E(B-V)[k(4686)-k(1640)]}, \quad (2)$$

where  $k(1640)$  and  $k(4686)$  are the absorption coefficients at 1640 and 4686 Å respectively. Rearranging Equation 2 for  $E(B - V)$  gives

$$E(B - V) = \frac{1}{0.4[k(4686) - k(1640)]} \log R_{\text{obs}} + \frac{1}{0.4[k(1640) - k(4686)]} \log R_0. \quad (3)$$

Here, we use the intrinsic ratio of  $\log R_0 = 0.89$  derived by Leitherer et al. (2019). We adopt the parameterization of Reddy et al. (2015) who expressed  $k(\lambda)$  as a third-order polynomial

$$k(\lambda) = -5.726 + \frac{4.004}{\lambda} - \frac{0.525}{\lambda^2} + \frac{0.029}{\lambda^3} + 2.505, \quad (4)$$

providing the absorption coefficients  $k(1640) = 8.249$  and  $k(4686) = 3.215$ . Applied to Equation (3), we obtain the relation

$$E(B - V)_{\text{He II}} = -0.497 \log R_{\text{obs}} + 0.442. \quad (5)$$

The measured He II ratios and the estimated  $E(B - V)_{\text{He II}}$  values are listed in Table 2.

##### 4.2. Reddening Estimates Based on the UV Slope

The attenuation values derived from the helium lines suggest that the UV wavelengths are strongly affected by dust. This makes the UV continuum a useful estimator of dust attenuation. The wavelength dependence of the UV continuum is well described by a power law. By measuring the spectral index  $\beta$  and comparing it to the intrinsic value, one can directly measure the dust attenuation  $E(B - V)_{\text{UV}}$ . Reddy et al. (2015) assumed an intrinsic continuum slope of  $-2.44$  and found a

relation between the UV dust attenuation and  $\beta$  of

$$E(B - V)_{\text{UV Slope}} = \frac{\beta + 2.44}{4.54}. \quad (6)$$

Measurement of the UV power-law indices for the STIS-observed star-forming regions is described in Section 2.2 and the  $\beta$ , as well as the  $E(B - V)_{\text{UV}}$  values, are listed in Table 2.

##### 4.3. Reddening Estimates Based on the Balmer Decrement

Following the same principle as for the He II lines, the Balmer lines can be used to measure dust attenuation. W-R emission lines and the UV continuum measured with  $\beta$  probe the attenuation of stellar light, whereas Balmer lines are of nebular origin, hence they probe dust attenuation in nebular regions. Furthermore, the Balmer line measurements are not always taken in the same aperture as the STIS observations, as described in detail in Section 3, and a comparison should therefore be taken with care.

To estimate the dust attenuation, we preferably use the ratio between the H $\alpha$  and H $\beta$  lines. However, for the galaxy Mrk 33, the H $\alpha$  line is saturated in the SDSS spectra, and we therefore use the line ratio between H $\beta$  and H $\gamma$ . For the dust attenuation we here assume an electron temperature of  $T_e = 10^4$  K and an electron density of  $n_e = 10^2 \text{ cm}^{-3}$  for Case B recombination as described in Osterbrock (1989). Following Momcheva et al. (2013) and Domínguez et al. (2013), the dust extinction estimate is based on the assumption of an intrinsic H $\alpha$ /H $\beta$  (or H $\beta$ /H $\gamma$ ) ratio of 2.86 (or 2.13) leading to

$$E(B - V)_{\alpha,\beta} = 1.97 \log \left[ \frac{(H\alpha/H\beta)_{\text{obs}}}{2.86} \right], \quad (7)$$

and

$$E(B - V)_{\beta,\gamma} = 4.43 \log \left[ \frac{(H\beta/H\gamma)_{\text{obs}}}{2.13} \right]. \quad (8)$$

The  $E(B - V)_{\text{Balmer}}$  values are listed in Table 2.

#### 5. Discussion

##### 5.1. Origin of Different Results between the Three Techniques

Overall, we find consistency between the different dust reddening estimates used in this work. The comparisons plotted in Figure 3 suggest good agreement between the three methods with the exception of the  $E(B - V)_{\text{UV}}$  estimate for NGC 3125. As discussed in the next section, there are reasons for the anomalous  $\beta$ -slope in this galaxy. Therefore we exclude NGC 3125 for the calculation of the correlation coefficients of all three combinations and find  $E(B - V)_{\text{He II}}$  versus  $E(B - V)_{\text{Balmer}} = 0.60$ ,  $E(B - V)_{\text{UV}}$  versus  $E(B - V)_{\text{Balmer}} = 0.69$ , and  $E(B - V)_{\text{UV}}$  versus  $E(B - V)_{\text{He II}} = 0.44$ . Although the statistical power of eight galaxies is limited, the results presented here suggest that the ratio of the He II lines can be used as an estimator of dust attenuation in star-forming regions beyond the Milky Way and the Magellanic Clouds.

However, differences in the determinations are expected due to their different physical origins and the different apertures used to measure  $E(B - V)_{\text{Balmer}}$ ,  $E(B - V)_{\text{He II}}$ , and  $E(B - V)_{\text{UV}}$ . As discussed in Leitherer et al. (2019), these three determinations of  $E(B - V)$  provide a unique opportunity to study the effects of dust at different ages and for the stellar and gas phase separately.

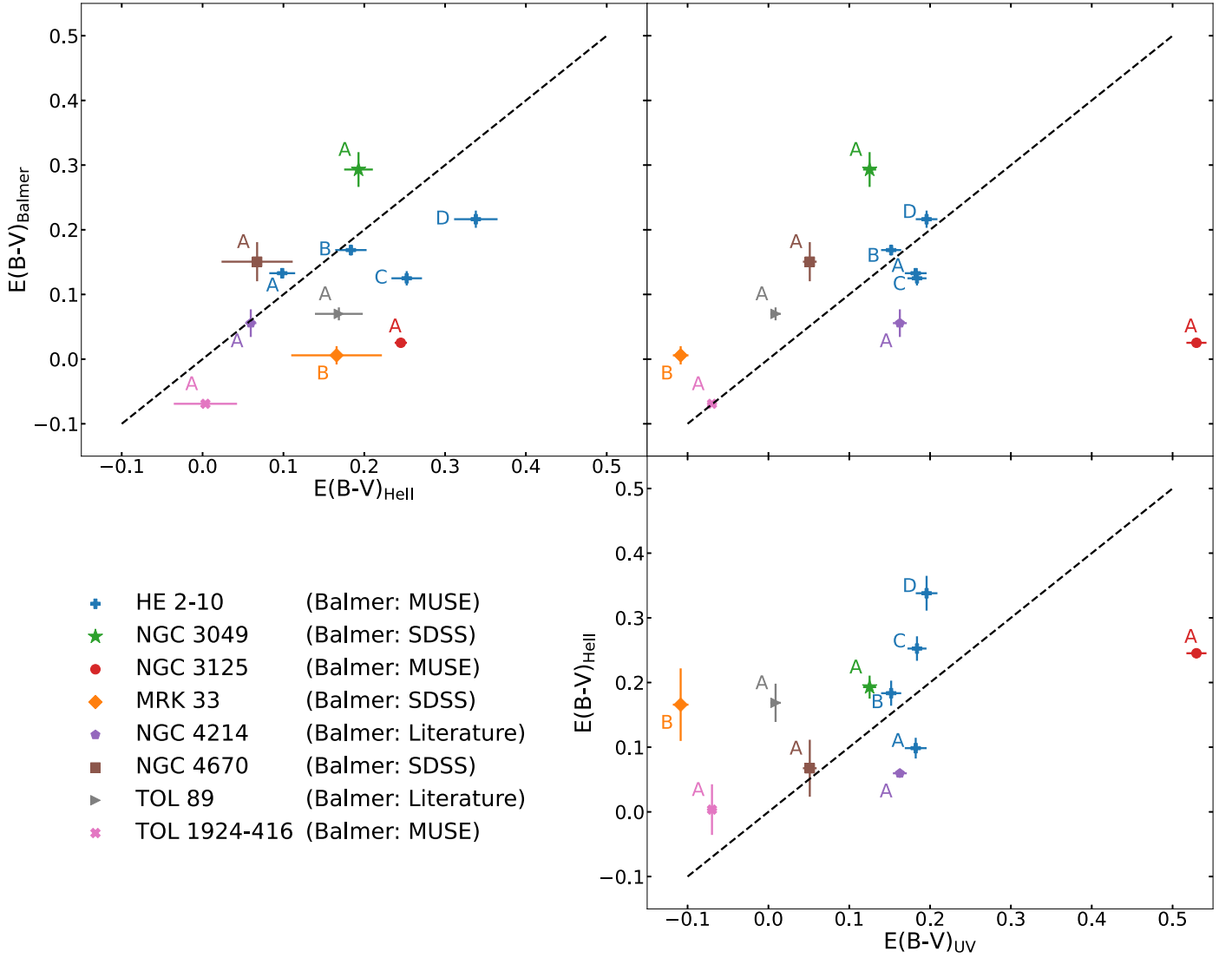


**Figure 3.** Comparison of all  $E(B-V)$  estimates computed in this work. A dashed line denotes the one-to-one relation. Each galaxy is represented by individual markers and colors. For some galaxies multiple clusters were identified and thus we specify each data point with a letter to cross-identify the measurement. The  $E(B-V)_{\text{Balmer}}$  measurements of the target sample are measured with the same method since we collected them from archival observations and literature values. The origin of the Balmer measurements are specified in the legend on the bottom left, and a detailed description of the data estimate is described in Section 3.

Is the dust attenuation of the gas different from that of the stars? As discussed in Calzetti et al. (1994), nebular emission from H II regions suffers about twice the amount of reddening experienced by the stellar continuum. This has been confirmed using large samples of nearby galaxies which show that  $A(\text{FUV})/A(\text{H}\alpha) = 1.8$  (e.g., Lee et al. 2009), as expected for the Calzetti reddening curve and differential extinction law (Calzetti 2001). However, the timescales of these tracers can be different by an order of magnitude, as the nebular Balmer recombination lines probe the dust attenuation of the gas at a characteristic age of  $\sim 5$  Myr, since only short-lived, massive stars emit sufficient Lyman-continuum radiation to create H II regions. With  $E(B-V)_{\text{HeII}}$  we can remove the age as a variable, and ask more directly whether the dust attenuation of the gas, as measured from the Balmer decrement, differs from that of the contemporaneous generation of stars, as measured by the W-R lines.

We calculate the mean reddening derived from the three methods, and obtain:

1.  $\overline{E(B-V)_{\text{HeII}}} = 0.15 \pm 0.09$ ,
2.  $\overline{E(B-V)_{\text{Balmer}}} = 0.12 \pm 0.10$ ,
3.  $\overline{E(B-V)_{\text{UV}}} = 0.09 \pm 0.11$ .

Even though these values agree with each other within their standard deviations, differences are tentatively present, suggesting the sequence  $E(B-V)_{\text{HeII}} > E(B-V)_{\text{Balmer}} > E(B-V)_{\text{UV}}$ . We caution against overinterpreting the significance of this relation, given the size of the statistical errors. In particular, the mean reddening derived from the Balmer lines must be taken with care, as the values were not obtained cospatially. Ignoring  $E(B-V)_{\text{Balmer}}$ , we can focus on  $E(B-V)_{\text{HeII}}$  and  $E(B-V)_{\text{UV}}$ , which are purely stellar-based dust tracers. Then this sequence can be understood by a relatively early onset of the clearing of natal material around the newly formed stars and a short (1–2 Myr) clearing timescale, consistent with previous studies of star formation timescales (e.g., Whitmore et al. 2011; Hollyhead et al. 2015; Sokal et al. 2016; Hannon et al. 2022). In fact, the different values would represent a sequence of reddening



estimates at different stages of stellar evolution, ranging from  $\sim 5$  Myr (W-R stars) to  $\sim 100$  Myr (B stars).

A further aspect which needs to be addressed is the production of dust due to W-R stars. As shown in Lau et al. (2020, 2022), carbon-rich W-R (WC) stars are a nonnegligible source of dust. However, the He II  $\lambda 1640$  and  $\lambda 4686$  lines are predominantly produced by WN stars with only a small contribution of WC stars. Therefore significant dust production by WC stars appears to be unlikely.

### 5.2. Comparison of Different Reddening in Individual Galaxies

In the following, we compare the different reddening estimates for individual galaxies and star-forming regions in our sample. The results are summarized in Figure 3. We note that for some galaxies not all observed regions have significant He II detection. In fact, for all nondetected regions we are unable to compute upper limits for the  $E(B - V)_{\text{He II}}$  values since both He II  $\lambda 1640$  and  $\lambda 4686$  are not detected.

*He 2-10.* This is the only galaxy in our sample with multiple detected He II emitters aligned in the STIS slit. The individual  $E(B - V)_{\text{He II}}$  values range from 0.10 mag (source A) to 0.34 mag (source D), suggesting that these four clusters are at different evolutionary stages. This is supported by the H $\alpha$  emission and dust, seen in the HST images (see Figure 1). Source D with the highest  $E(B - V)_{\text{He II}}$  value is visibly affected by diffuse strong H $\alpha$  emission situated to its east. For sources A–C most of the dust and gas has already been displaced and a cavity has been created in the ISM by star formation feedback. However, their  $E(B - V)_{\text{Balmer}}$  and  $E(B - V)_{\text{UV}}$  values do not show such strong variation. Overall these values are in good agreement with each other. This might be due to the fact that the spatial resolution of the MUSE observation is not enough to resolve each individual source (see Section 3.1).

*Mrk 33.* This galaxy has two bright star clusters aligned within the slit but only source B has detected He II lines. The estimate of  $E(B - V)_{\text{Balmer}}$  was done with Balmer lines measured by SDSS with an aperture ( $3''$ ) covering both sources. The UV and Balmer measurements suggest the absence of dust, whereas the He II measurement deviates from this with a dust attenuation of  $E(B - V)_{\text{He II}} = 0.17 \pm 0.06$  mag. By studying the morphology of Source B in Figure 1, we find that the cluster itself has no strong H $\alpha$  emission, indicating that star formation feedback has already pushed away dust and gas.

*NGC 3049.* We find good agreement between the He II and UV dust reddening estimates for Source A. Source B has no significant He II emission but we derived an  $E(B - V)_{\text{UV}}$  value of 0.42 mag. This value is significantly higher than for Source A (0.13 mag) and might be the reason for the nondetection of the He II lines due to dust attenuation. However, we do not see any traces of nebular H $\alpha$  emission around source B, which might be due to the fact that this source is already older than  $\sim 5$  Myr and the W-R star population has already disappeared. The dust reddening estimated from SDSS Balmer line measurements of  $E(B - V)_{\text{Balmer}} = 0.29$  mag is in between the UV-estimated values of Sources A and B. This might be the result of blending of both sources within the SDSS fiber.

*NGC 3125.* Source A in NGC 3125 is the most discrepant data point in Figure 3. While the  $E(B - V)_{\text{Balmer}}$  values determined from the Balmer lines and from He II agree reasonably well, the  $E(B - V)_{\text{UV}}$  value from the UV slope

disagrees. The UV value of  $E(B - V)_{\text{UV}} = 0.53$  mag significantly exceeds the results obtained via the other two methods. Inspection of the spectrum taken with the Cosmic Origin Spectrograph (COS) confirms a very red UV slope and therefore high reddening. Chandar et al. (2004) pointed out the unusually high equivalent width of He II  $\lambda 1640$  in NGC 3125-A and proposed a scenario of a large population of W-R stars in conjunction with a dust morphology resulting in larger dust attenuation for the W-R population than for the OB population responsible for the stellar continuum. The peculiar shape of the UV continuum is evident in large-aperture ( $20'' \times 10''$ ) spectroscopic observations obtained with the International Ultraviolet Explorer (Kinney et al. 1993). The UV spectrum of NGC 3125 is steeply rising from 2200 to 1700 Å with an essentially flat continuum at shorter wavelengths. The flat wavelength region is used for determining  $\beta$  in the current work. This bimodal continuum shape is most pronounced in NGC 3125 compared to other galaxies in the atlas of Kinney et al. (1993).

Wofford et al. (2023) found evidence of very massive stars having initial masses of up to  $300 M_{\odot}$  in NGC 3125-A. Such stars mimic the spectral features of classical W-R stars but are otherwise still core-hydrogen burning main-sequence stars. The detection of highly excited O V  $\lambda 1371$  by Wofford et al. (2023) is consistent with these stars being hot ( $T_{\text{eff}} \approx 50,000$  K) and luminous ( $L \approx 10^7 L_{\odot}$ ). If so, they would be a significant source of hydrogen-ionizing photons. The additional supply of ionizing photons will enhance the nebular contribution to the spectral energy distribution. Of particular interest in this context is the wavelength region around 1500 Å, where the energy flux of the two-photon continuum peaks (Johnstone et al. 2012). A stronger two-photon continuum will redden the total (stellar + nebular) continuum. Consequently, the flat spectral slope observed in NGC 3125-A could result from the presence of very massive stars whose ionizing photon output increases the nebular continuum in the UV.

*NGC 4214.* The broad He II emitter in NGC 4214 is characterized by a distinct bubble structure of hydrogen around this source. This is most likely formed from star formation feedback associated with this source as this is the most luminous source in this region (see Figure 1). We find good agreement between all three measurements, keeping in mind that the measurement of the Balmer lines was taken for the entire galaxy (Moustakas & Kennicutt 2006). However, the H II region hosting the W-R stars is clearly the brightest source and might dominate the ionized gas spectra, resulting in similar  $E(B - V)$  values.

*NGC 4670.* Even though three sources were found in NGC 4670, only Source A has significant He II emission. The SDSS spectroscopic fiber is centered on Source A, which is the brightest optical source in this region, presumably dominating the SDSS spectrum. This source is also characterized by a negligibly small dust attenuation estimate whose values agree within the errors for the three methods.

*Tol 1924-416.* This is a bright source with no significant direct neighbor. This makes it very suitable for our Balmer line measurement with the archival MUSE observation. Interestingly this source appears to have ejected all its dusty envelope since we do not detect any dust attenuation with all three of the used methods.

*Tol 89.* This is the only source which has been observed with a Balmer line estimate of comparable aperture by Sidoli et al. (2006).

The UV slope is very blue, indicative of little dust attenuation ( $E(B - V)_{\text{UV}} = 0.01$  mag), whereas the Balmer and He II line ratios indicate dust attenuation of 0.17 and 0.07 mag, respectively. The morphology as seen in Figure 1 does also not indicate a large dust content.

### 5.3. Further Application in Different Redshift Regimes

Two follow-up projects to our pilot analysis of broad He II lines are desirable: first, more rigorous testing with better statistics in the local Universe, accompanied by an extended study of the emitter's properties, would help to put this dust tracer for young ( $< 5$  Myr) stellar populations on a firmer footing. Subsequently, we can apply this method to targets at higher redshift to probe the dust reddening in starburst regions beyond the local Universe. In the following we will discuss available data and also the feasibility in different redshift regimes.

The challenge to observing broad He II lines in the local Universe is the need for space-based spectroscopy for the He II  $\lambda 1640$  line. A well-suited HST program is the COS Legacy Archive Spectroscopic SurveY (CLASSY), as it provides a UV spectral database of 45 nearby ( $0.002 < z < 0.182$ ) galaxies with dust reddening values of  $0.02 < E(B - V) < 0.67$  (Berg et al. 2022). HST/COS observes targets with a  $2''.5$  circular aperture. This survey has the distinct advantage that it provides high-quality ( $S/N_{1500\text{\AA}} \gtrsim 5/\text{resel}$ ) and high-resolution ( $R \sim 15,000$ ; James et al. 2022) spectra which are ideal in order to search for broad He II emitters. CLASSY has a broad range of galaxy types, but is biased toward UV-bright star-forming galaxies. The survey covers stellar masses ranging over  $\log(M_*) \sim 6-10M_\odot$ , star formation rates of  $\log(\text{SFR}) \sim -2$  to  $+2 M_\odot \text{ yr}^{-1}$ , and oxygen abundances of  $12 + \log(\text{O}/\text{H}) \sim 7-9$  (Berg et al. 2022). The CLASSY sample also provides optical spectra for all targets covering the optical He II  $\lambda 4686$  line. The optical spectra are collected from archival data including SDSS, VLT/VIMOS integral field unit (IFU), MMT Blue Channel Spectrograph, Keck/KCWI IFU, Keck/ESI, and VLT/MUSE IFU. As discussed in Arellano-Córdova et al. (2022), SDSS and COS have different apertures of  $3''$  and  $2''.5$ , respectively. The spectra obtained with the MMT Blue Channel Spectrograph and KECK/ESI have a long-slit aperture width of  $1''$ . The spectra taken from IFUs on the other hand are extracted in a  $2''.5$  aperture. Even though not all optical spectra were obtained with the exact same aperture as the one with COS, we can assume that broad He II lines originate from only one dominating stellar population. Significant broad He II  $\lambda 1640$  has been reported in one galaxy (J0127-0619 or Mrk 996)

The CLASSY sample stands out due to its good spectral coverage and sample size and is therefore well suited for an extended search for broad He II  $\lambda 1640$  emitters. Senchyna et al. (2021) discuss a sample of 10 local star-forming galaxies with available UV and optical spectroscopy. Broad W-R features have been detected in all 10 galaxies. This sample could be an obvious extension of the sample of eight presented here. A systematic search for broad He II  $\lambda 4686$  lines in SDSS data release 6 was performed by Brinchmann et al. (2008), resulting in 570 galaxies with significant W-R line detections and further 1115 potential candidates. This sample can be used as a basis of future UV observations, providing He II  $\lambda 1640$  line measurements.

For galaxies at a redshift  $z \gtrsim 1.0$  the He II  $\lambda 1640$  line is observable at optical wavelengths (at  $z = 1.0$ , He II  $\lambda 1640$  is observed at  $\sim 3300 \text{ \AA}$ ), and can in principle be obtained from the ground. In order to explore the detection of He II lines in galaxies at higher redshift, we project observed fluxes for the galaxy NGC 3125 to higher distances. This galaxy is the brightest known He II  $\lambda 1640$  emitter in the local Universe (Chandar et al. 2004). This source has observed He II  $\lambda 1640$  and  $\lambda 4686$  line fluxes of  $23.76 \pm 1.1 \times 10^{-15} \text{ erg s}^{-1} \text{ cm}^{-2}$  and  $9.59 \pm 0.3 \times 10^{-15} \text{ erg s}^{-1} \text{ cm}^{-2}$ , respectively. By using the relation between luminosity  $L$  and observed flux  $F$

$$L = 4\pi F D_L, \quad (9)$$

where  $D_L$  is the luminosity distance, we can assume that such a source with the same luminosity has a predicted flux at a given redshift of

$$F(z) = \frac{F(z = 0.0037) \times D_L(z = 0.0037)^2}{D_L(z)^2}. \quad (10)$$

This leads to predicted fluxes of  $13.7 \times 10^{-20} \text{ erg s}^{-1} \text{ cm}^{-2}$  and  $5.5 \times 10^{-20} \text{ erg s}^{-1} \text{ cm}^{-2}$  for the He II  $\lambda 1640$  and  $\lambda 4686$  lines, respectively, at a redshift of  $z = 1.0$ . State-of-the-art spectrographs mounted on large telescopes like the VLT are, however, not capable of detecting He II lines. As an example, we estimated S/N values of the He II  $\lambda 1640$  and the  $\lambda 4686$  of  $\sim 10^{-5} \text{ pixel}^{-1}$  for a 1 hr VLT/XSHOOTER observation,<sup>5</sup> as this instrument provides the needed spectral coverage and resolution.

By stacking spectra, broad He II  $\lambda 1640$  W-R features were observed in  $z \sim 3$  LBGs ( $N \sim 1000$ ; Shapley et al. 2003), in star-forming galaxies at  $z = 2.40 \pm 0.11$  ( $N \sim 30$ ; Steidel et al. 2016), and in highly magnified gravitationally lensed galaxies at redshifts  $1.6 < z < 3.6$  ( $N \sim 14$ ; Rigby et al. 2018). In Saxena et al. (2020), six broad He II  $\lambda 1640$  emitters at a mean redshift of  $z = 2.7$  using VLT/VIMOS were detected with fluxes between  $2.0$  and  $23.1 \times 10^{-18} \text{ erg s}^{-1} \text{ cm}^{-2}$ . However, given the fact that these observations only have an S/N ratio between 2 and 7 and that for these sources the He II  $\lambda 4686$  is shifted into near-infrared wavelengths, it is likely that this line remains undetectable at these redshifts from the ground. With current technology it is not possible to make a positive prediction at what distance the He II line ratio can be used as dust reddening tracers. Therefore, the most promising strategy would be to first extend its limit in the local Universe and test this method using targets up  $\sim 100 \text{ Mpc}$  using space-based UV observations.

## 6. Conclusion

We discuss a novel method to determine the dust attenuation in star-forming galaxies containing W-R stars. We applied the stellar He II  $\lambda 1640$  to  $\lambda 4686$  line ratio as a dust reddening tracer to a sample of eight galaxies. We measured the fluxes of these lines with HST/STIS long-slit observations in the UV and optical, respectively. Both measurements were taken at the same position and aperture to guarantee cospatial observations. As this is the first application of this method, we compared our dust reddening estimates to two commonly used methods. We measured the UV slope from HST/STIS observations and

<sup>5</sup> We used the ESO exposure time calculator <https://www.eso.org/observing/etc/>.

collected Balmer line measurements for all eight galaxies from the literature. We find consistency between the three methods except for NGC 3125, which we interpret as due to an exceptional contribution from a nebular continuum affecting the UV continuum. Even though the Balmer line measurements are not always cospatial with the HST/STIS observations, we still find a significant correlation with the UV and He II methods. This is most likely due to the fact that the selected sources for this study are all bright young star clusters which dominate the luminosity of their local environment. We find tentative evidence for offsets between the reddening values derived from the three methods: the He II method suggests the largest values, with the UV method leading to the lowest reddening. As these dust reddening estimates probe different age regimes, we may witness different stages of dust clearing. This pilot study is still limited by small number statistics, and an expanded data set is needed. Suitable data sets exist for galaxies in the local Universe, and there are opportunities for extending this method to more galaxies at larger distances.

### Acknowledgments

This research is based on observations made with the NASA/ESA Hubble Space Telescope obtained from the Space Telescope Science Institute, which is operated by the Association of Universities for Research in Astronomy, Inc., under NASA contract NAS 5-26555. These observations are associated with programs 9036, 7513, 15846, 06580, 11146, 11987, 10400, 11360, 06639, and 06708. Support for this work has been provided by NASA through grant Nos. AR-15036 and GO-15846. Some of the data presented in this article were obtained from the Mikulski Archive for Space Telescopes (MAST) at the Space Telescope Science Institute. The specific observations analyzed can be accessed via doi:10.17909/3721-pj98.

Based on observations collected at the European Southern Observatory under ESO programs 095.B-0321 (PI: Vanzi), 094.B-0745 (Garcia-Benito, Ruben), and 60.A-9314 (MUSE Science Verification).

This research has made extensive use of the NASA/IPAC Extragalactic Database (NED) which is operated by the Jet Propulsion Laboratory, California Institute of Technology, under contract with the National Aeronautics and Space Administration.

Funding for the Sloan Digital Sky Survey IV has been provided by the Alfred P. Sloan Foundation, the U.S. Department of Energy Office of Science, and the Participating Institutions.

SDSS-IV acknowledges support and resources from the Center for High Performance Computing at the University of Utah. The SDSS website is [www.sdss4.org](http://www.sdss4.org).

SDSS-IV is managed by the Astrophysical Research Consortium for the Participating Institutions of the SDSS Collaboration including the Brazilian Participation Group, the Carnegie Institution for Science, Carnegie Mellon University, Center for Astrophysics|Harvard & Smithsonian, the Chilean Participation Group, the French Participation Group, Instituto de Astrofísica de Canarias, the Johns Hopkins University, Kavli Institute for the Physics and Mathematics of the Universe (IPMU)/University of Tokyo, the Korean Participation Group, Lawrence Berkeley National Laboratory, Leibniz Institut für Astrophysik Potsdam (AIP), Max-Planck-Institut für Astronomie (MPIA Heidelberg), Max-Planck-Institut für Astrophysik (MPA

Garching), Max-Planck-Institut für Extraterrestrische Physik (MPE), National Astronomical Observatories of China, New Mexico State University, New York University, University of Notre Dame, Observatório Nacional/MCTI, The Ohio State University, Pennsylvania State University, Shanghai Astronomical Observatory, United Kingdom Participation Group, Universidad Nacional Autónoma de México, University of Arizona, University of Colorado Boulder, University of Oxford, University of Portsmouth, University of Utah, University of Virginia, University of Washington, University of Wisconsin, Vanderbilt University, and Yale University.


*Software:* astropy (Astropy Collaboration et al. 2013, 2018, 2022), specutils (Earl et al. 2023), calstis (Sohn 2019), matplotlib (Hunter 2007), and numpy (Harris et al. 2020).

### ORCID iDs

Daniel Maschmann  <https://orcid.org/0000-0001-6038-9511>

Claus Leitherer  <https://orcid.org/0000-0003-2685-4488>

Andreas L. Faist  <https://orcid.org/0000-0002-9382-9832>

Janice C. Lee  <https://orcid.org/0000-0002-2278-9407>

### References

- Arellano-Córdova, K. Z., Mingozzi, M., Berg, D. A., et al. 2022, *ApJ*, **935**, 74
- Astropy Collaboration, Price-Whelan, A. M., Lim, P. L., et al. 2022, *ApJ*, **935**, 167
- Astropy Collaboration, Price-Whelan, A. M., Sipőcz, B. M., et al. 2018, *AJ*, **156**, 123
- Astropy Collaboration, Robitaille, T. P., Tollerud, E. J., et al. 2013, *A&A*, **558**, A33
- Berg, D. A., James, B. L., King, T., et al. 2022, *ApJS*, **261**, 31
- Brinchmann, J., Kunth, D., & Durret, F. 2008, *A&A*, **485**, 657
- Calzetti, D. 2001, *PASP*, **113**, 1449
- Calzetti, D. 2009, Dust in External Galaxies, in ASP Conf. Ser. 414, Cosmic Dust—Near and Far, ed. T. Henning, E. Grün, & J. Steinacker (San Francisco, CA: ASP), 214
- Calzetti, D., Kinney, A. L., & Storchi-Bergmann, T. 1994, *ApJ*, **429**, 582
- Cardelli, J. A., Clayton, G. C., & Mathis, J. S. 1989, *ApJ*, **345**, 245
- Chandar, R., Leitherer, C., & Tremonti, C. A. 2004, *ApJ*, **604**, 153
- Chandar, R., Leitherer, C., Tremonti, C. A., et al. 2005, *ApJ*, **628**, 210
- Conti, P. S., Garmany, C. D., De Loore, C., & Vanbeveren, D. 1983, *ApJ*, **274**, 302
- Conti, P. S., & Morris, P. W. 1990, *AJ*, **99**, 898
- Crowther, P. A. 2007, *ARA&A*, **45**, 177
- Crowther, P. A., & Hadfield, L. J. 2006, *A&A*, **449**, 711
- Domínguez, A., Siana, B., Henry, A. L., et al. 2013, *ApJ*, **763**, 145
- Drout, M. R., Götzberg, Y., Ludwig, B. A., et al. 2023, arXiv:2307.00061
- Earl, N., Tollerud, E., O’Steen, R., et al., 2023 astropy/specutils: v1.12.0, Zenodo, doi:10.5281/zenodo.10016569
- Eldridge, J. J., Stanway, E. R., Xiao, L., et al. 2017, *PASA*, **34**, e058
- Fitzpatrick, E. L. 1986, *AJ*, **92**, 1068
- González Delgado, R. M., Leitherer, C., Stasińska, G., & Heckman, T. M. 2002, *ApJ*, **580**, 824
- Götzberg, Y., Drout, M. R., Ji, A. P., et al. 2023, *ApJ*, **959**, 125
- Hannon, S., Lee, J. C., Whitmore, B. C., et al. 2022, *MNRAS*, **512**, 1294
- Harris, C. R., Millman, K. J., van der Walt, S. J., et al. 2020, *Natur*, **585**, 357
- Hillier, D. J. 1987, *ApJS*, **63**, 965
- Hollyhead, K., Bastian, N., Adamo, A., et al. 2015, *MNRAS*, **449**, 1106
- Hummer, D. G., & Storey, P. J. 1987, *MNRAS*, **224**, 801
- Hunter, J. D. 2007, *CSE*, **9**, 90
- James, B. L., Berg, D. A., King, T., et al. 2022, *ApJS*, **262**, 37
- Johnstone, R. M., Canning, R. E. A., Fabian, A. C., et al. 2012, *MNRAS*, **425**, 1421
- Kinney, A. L., Bohlin, R. C., Calzetti, D., Panagia, N., & Wyse, R. F. G. 1993, *ApJS*, **86**, 5
- Lau, R. M., Eldridge, J. J., Hankins, M. J., et al. 2020, *ApJ*, **898**, 74
- Lau, R. M., Hankins, M. J., Han, Y., et al. 2022, *NatAs*, **6**, 1308
- Lee, J. C., Gil de Paz, A., Tremonti, C., et al. 2009, *ApJ*, **706**, 599



- Leitherer, C., Ekström, S., Meynet, G., et al. 2014, [ApJS](#), **212**, 14
- Leitherer, C., Lee, J. C., & Faisst, A. 2019, [AJ](#), **158**, 192
- Meynet, G., & Maeder, A. 2005, [A&A](#), **429**, 581
- Meynet, G., Maeder, A., Georgy, C., et al. 2017, Massive stars, successes and challenges, in IAU Symp. 329, The Lives and Death-Throes of Massive Stars, 329, ed. J. Eldridge, J. Bray, L. McClelland et al., **3**
- Mokiem, M. R., de Koter, A., Vink, J. S., et al. 2007, [A&A](#), **473**, 603
- Momcheva, I. G., Lee, J. C., Ly, C., et al. 2013, [AJ](#), **145**, 47
- Moustakas, J., & Kennicutt, R. C., Jr. 2006, [ApJS](#), **164**, 81
- Osterbrock, D. E. 1989, Astrophysics of Gaseous Nebulae and Active Galactic Nuclei (Mill Valley, CA: University Science Books)
- Reddy, N. A., Kriek, M., Shapley, A. E., et al. 2015, [ApJ](#), **806**, 259
- Rigby, J. R., Bayliss, M. B., Chisholm, J., et al. 2018, [ApJ](#), **853**, 87
- Salim, S., Boquien, M., & Lee, J. C. 2018, [ApJ](#), **859**, 11
- Saxena, A., Pentericci, L., Mirabelli, M., et al. 2020, [A&A](#), **636**, A47
- Schaerer, D. 1996, [ApJL](#), **467**, L17
- Schaerer, D., & Vacca, W. D. 1998, [ApJ](#), **497**, 618
- Senchyna, P., Stark, D. P., Charlot, S., et al. 2021, [MNRAS](#), **503**, 6112
- Shapley, A. E., Steidel, C. C., Pettini, M., & Adelberger, K. L. 2003, [ApJ](#), **588**, 65
- Shirazi, M., & Brinchmann, J. 2012, [MNRAS](#), **421**, 1043
- Sidoli, F., Smith, L. J., & Crowther, P. A. 2006, [MNRAS](#), **370**, 799
- Sohn, T. S. 2019, STIS Data Handbook, Vol. 7 (Baltimore, MD: STScI)
- Sokal, K. R., Johnson, K. E., Indebetouw, R., & Massey, P. 2016, [ApJ](#), **826**, 194
- Steidel, C. C., Strom, A. L., Pettini, M., et al. 2016, [ApJ](#), **826**, 159
- van der Hucht, K. A. 2001, [NewAR](#), **45**, 135
- Whitmore, B. C., Chandar, R., Kim, H., et al. 2011, [ApJ](#), **729**, 78
- Wofford, A., Sixtos, A., Charlot, S., et al. 2023, [MNRAS](#), **523**, 3949
- Xiao, L., Stanway, E. R., & Eldridge, J. J. 2018, [MNRAS](#), **477**, 904